

On the robustness of inverse scattering for penetrable, homogeneous objects with complicated boundary

Carlos Borges* Manas Rachh† Leslie Greengard‡

October 24, 2022

Abstract

The acoustic inverse obstacle scattering problem consists of determining the shape of a domain from measurements of the scattered far field due to some set of incident fields (probes). For a penetrable object with known sound speed, this can be accomplished by treating the boundary alone as an unknown curve. Alternatively, one can treat the entire object as unknown and use a more general *volumetric* representation, without making use of the known sound speed. Both lead to strongly nonlinear and nonconvex optimization problems for which recursive linearization provides a useful framework for numerical analysis. After extending our shape optimization approach developed earlier for impenetrable bodies, we carry out a systematic study of both methods and compare their performance on a variety of examples. Our findings indicate that the volumetric approach is more robust, even though the number of degrees of freedom is significantly larger. We conclude with a discussion of this phenomenon and potential directions for further research.

Keywords: Inverse scattering, transmission problem, Helmholtz equation, boundary integral equations, recursive linearization.

1 Introduction

Using waves as probes for non-destructive or non-invasive testing is of interest in a diverse set of applications, from medical imaging to materials characterization, remote sensing, sonar and radar [47, 29, 34, 56, 28, 14, 45, 55]. With acoustic waves, one can imagine recovering the shape, density, and/or internal sound speed from measurements of the scattered field induced by a collection of known incident waves. In this paper, we focus on recovering the shape Γ of a penetrable obstacle Ω_i with known density ρ_i and sound speed c_i immersed in a medium $\Omega_e = \mathbb{R}^2 \setminus \Omega_i$ with density ρ_e and sound speed c_e , assuming the data consists of far field measurements when a plane wave impinges on the unknown obstacle from multiple directions at multiple frequencies. We will refer to this as the *inverse penetrable obstacle problem* or simply the *inverse obstacle problem*. The incident wave at frequency ω will be denoted by u^{inc} , the field in the interior will be denoted by u_i and

*Department of Mathematics, University of Central Florida, Orlando, FL, USA. *Email:* carlos.borges@ucf.edu

†Flatiron Institute, New York, NY, USA. *Email:* mrachh@flatironinstitute.org

‡Courant Institute of Mathematical Sciences, New York University, New York, NY, USA and Flatiron Institute, New York, NY, USA. *Email:* greengard@cims.nyu.edu

the scattered field will be denoted by u_e . The total field u is equal to u_i in the interior and to the sum $u^{inc} + u_e$ in the exterior. The corresponding (time harmonic) forward problem at frequency ω consists of solving

$$\begin{cases} \Delta u_i + k_i^2 u_i = 0, & \text{in } \Omega_i, \\ \Delta u_e + k^2 u_e = 0, & \text{in } \Omega_e, \\ [u] = 0 \text{ and } [\beta \frac{\partial u}{\partial \nu}] = 0, & \text{on } \Gamma, \\ \lim_{\|\mathbf{x}\| \rightarrow \infty} \|\mathbf{x}\|^{1/2} \left(\frac{\partial u_e}{\partial r} - i k u_e \right) = 0. \end{cases} \quad (1)$$

assuming the density and sound speed are known. Here, $k = \omega/c_e$ is the wavenumber in the exterior medium and $k_i = \omega/c_i$ is the wavenumber in the interior of the obstacle, $[u] = u|_+ - u|_-$, with $u|_+$ and $u|_-$ denoting the limit of the total field as one approaches Γ from the exterior and interior, respectively. β is a piecewise constant function with $\beta = 1$ in Ω_e and $\beta = \rho_e/\rho_i$ in Ω_i . The direction of the incident plane wave will be denoted by the unit vector $\boldsymbol{\theta}$, so that $u^{inc}(\mathbf{x}) = e^{ik\mathbf{x}\cdot\boldsymbol{\theta}}$. The solution to (1) can be obtained using a boundary integral equation method [44, 41, 39, 30, 53] with two unknown source densities supported on Γ alone. The obstacle problem and the integral equation approach are described in section 2.

Alternatively, one can treat the domain as having an unknown shape defined by the (compact) support of some perturbation, $q(x)$, of the sound speed in the ambient space. We will refer to this as the *inverse medium problem* [31]. The forward problem here consists of computing the scattered field u^{scat} induced by the same incident wave u^{inc} as above when it impinges on the obstacle defined by a *known* function $q(x)$:

$$\begin{cases} \Delta u^{scat} + k^2(1+q)u^{scat} = -k^2 q u^{inc}, & \text{in } \mathbb{R}^2, \\ \lim_{\|\mathbf{x}\| \rightarrow \infty} \|\mathbf{x}\|^{1/2} \left(\frac{\partial u^{scat}}{\partial r} - i k u^{scat} \right) = 0. \end{cases} \quad (2)$$

While problem (2), like problem (1), can be solved using integral equation techniques, the scattered field must now be represented as a volume potential, leading to the Lippmann-Schwinger integral equation [31]. This approach is discussed in section 3.

Remark 1.1. *If $\rho_i = \rho_e$ in problem (1), the support of the function q is defined to be Ω_i , and $k_i^2 = k^2(1+q)$ inside Ω_i , then the two forward problems are identical.*

Suppose now that a collection of N_r receivers are equispaced on a disk of radius $R \gg 1$: $\{\mathbf{r}_m = (R \cos \frac{2\pi m}{N_r}, R \sin \frac{2\pi m}{N_r}), m = 1, 2, \dots, N_r\}$. We then define the forward transmission operator by

$$\mathcal{F}_{k,\boldsymbol{\theta}}^{(T)}(\Gamma) = \mathbf{u}_{k,\boldsymbol{\theta}}^{meas} \in \mathbb{C}^{N_r}, \quad (3)$$

where the m th component of $\mathbf{u}_{k,\boldsymbol{\theta}}^{meas}$ is the scattered field $u_e(\mathbf{r}_m)$, that solves (1) in response to an incoming plane wave $u^{inc}(\mathbf{x}) = e^{ik\mathbf{x}\cdot\boldsymbol{\theta}}$. The inverse obstacle problem can now be stated more precisely in terms of optimization, namely in the form

$$\tilde{\Gamma} = \arg \min_{\Gamma} \sum_{k_l, \boldsymbol{\theta}_j} \|\mathbf{u}_{k_l, \boldsymbol{\theta}_j}^{meas} - \mathcal{F}_{k_l, \boldsymbol{\theta}_j}^{(T)}(\Gamma)\|, \quad (4)$$

assuming we have N_k probing frequencies $\{k_1, \dots, k_{N_k}\}$ and N_d incident directions $\{\boldsymbol{\theta}_1, \dots, \boldsymbol{\theta}_{N_k}\}$.

Similarly, the forward volumetric scattering operator is defined by

$$\mathcal{F}_{k,\boldsymbol{\theta}}^{(V)}(q) = \mathbf{u}_{k,\boldsymbol{\theta}}^{meas} \in \mathbb{C}^{N_r}, \quad (5)$$

where the m th component of $\mathbf{u}_{k,\boldsymbol{\theta}}^{meas}$ is the scattered field $u^{scat}(\mathbf{r}_m)$ that solves (2), in response to an incoming plane wave $u^{inc}(\mathbf{x}) = e^{i\mathbf{k}\mathbf{x}\cdot\boldsymbol{\theta}}$ impinges on the inhomogeneity. The inverse medium problem can be stated in the form

$$\tilde{q} = \arg \min_q \sum_{k_l, \boldsymbol{\theta}_j} \|\mathbf{u}_{k_l, \boldsymbol{\theta}_j}^{meas} - \mathcal{F}_{k_l, \boldsymbol{\theta}_j}^{(V)}(q)\|. \quad (6)$$

The inverse problems (4) and (6) are fully nonlinear, ill-posed without additional constraints, and computationally challenging. A variety of nonlinear iterations have been applied to such problem, including the Gauss-Newton method [31], other Newton-like variants, Landweber iteration, and the nonlinear conjugate gradient method [43, 46]. To deal with the ill-posedness, regularization methods such as Tikhonov regularization or the truncated SVD can be used. Alternatively, one can use a parametric approximation of the object with fewer degrees of freedom in the forward model. One such approximation is to assume that the object is bandlimited, with the bandlimit determined by the frequency and the number of independent measurements. Finally, one can either choose to solve for the unknown object using all frequencies simultaneously or solve a sequence of single frequency inverse problems. Since using all frequencies together is computationally expensive, Chen [25, 26] suggested the recursive linearization algorithm (RLA). In this approach, one first solves for a low-resolution approximation of the unknown using only the lowest frequency data. This reconstruction then serves as an initial guess for Gauss-Newton iteration at the next available frequency, until the highest frequency data has been reached. At each step of this iteration, the complexity of the unknown is gradually increased, typically by increasing its bandlimit. The RLA has been successfully applied to both inverse obstacle scattering and the inverse medium problem [4, 5, 11, 7, 8, 9, 10, 15, 21, 16, 54, 18]. We refer the reader to [6] for a thorough review of inverse scattering problems based on multiple frequency data.

The present paper is aimed at a question that appears not to have been considered previously: namely, to compare inverse obstacle scattering and the inverse medium problem as numerical approaches when the forward problems are identical, as outlined above. In section 2, after reviewing integral equation methods for forward scattering from a penetrable obstacle, we extend the recursive linearization method of [54, 16, 18] for sound-soft obstacles to the current setting. Next, we briefly review the volumetric inverse scattering method (also based on recursive linearization) presented in [15]. Both methods have been shown to be capable of obtaining high resolution reconstructions of very complicated, but suitably bandlimited, unknowns. Focusing on computational complexity, it is straightforward to see that the inverse obstacle approach should be much faster. Boundary integral methods are used for the forward scattering problem and only an unknown curve is being sought. The volumetric inverse scattering approach requires volume integral equations to be solved and seeks an unknown function defined on a two-dimensional region in the plane.

Note, however, that the formulations have distinct features, ignoring questions of computational efficiency. First, the obstacle scattering approach is seeking a discontinuity in sound speed defined on a smooth curve, while the volumetric scattering approach is seeking a smooth (bandlimited) function with the same scattered far field. It is easy to imagine that this affects the robustness of the solver, the dependence on the number of measurements, etc. We will explore these questions numerically in section 4. An interesting discovery is that there are clear cases where the volumetric approach is able to obtain high quality reconstruction while the obstacle approach fails. We conclude with a discussion of these results and opportunities for further research in section 5.

Remark 1.2. *Since the data sets are somewhat complicated, and depend on several parameters, we summarize some of the important notation in Table 1. When the context is clear, we will omit*

Table 1: List of principal symbols used in this article.

Symbol	Description
Ω_i	interior of the penetrable obstacle
Ω_e	exterior of the penetrable obstacle
Γ	boundary of Ω_i
q	perturbation of the sound speed in Ω_i
ω	frequency of the incident plane wave
k	wavenumber of the incident plane wave in Ω_e
k_i	wavenumber of the incident plane wave in Ω_i
\mathbf{r}_j	location of j th receiver in Ω_e
$\boldsymbol{\theta}$	incident direction of plane wave $u_{k,\boldsymbol{\theta}}^{inc}$ ($\ \boldsymbol{\theta}\ = 1$)
$u_{k,\boldsymbol{\theta}}^{inc}$	incident plane wave with wavenumber k and direction $\boldsymbol{\theta}$
$u_{k,\boldsymbol{\theta}}^{scat}$	scattered field generated by $u_{k,\boldsymbol{\theta}}^{inc}$
$\mathbf{u}_{k,\boldsymbol{\theta}}^{meas}$	vector in \mathbb{C}^{N_r} , with j th component $u_{k,\boldsymbol{\theta}}^{scat}(\mathbf{r}_j)$
N_k	number of probing frequencies
N_r	number of receivers
N_d	number of incident waves
$\mathcal{F}_{k,\boldsymbol{\theta}}^{(V)}$	forward operator for volume scattering mapping q in Ω_i to $\mathbf{u}_{k,\boldsymbol{\theta}}^{meas}$ (for given $u_{k,\boldsymbol{\theta}}^{inc}$)
$\mathcal{F}_{k,\boldsymbol{\theta}}^{(T)}$	forward operator for obstacle scattering mapping $\partial\Omega$ to $\mathbf{u}_{k,\boldsymbol{\theta}}^{meas}$ (for given $u_{k,\boldsymbol{\theta}}^{inc}$)
$\mathcal{J}_{k,\boldsymbol{\theta}}^{(V)}$	Fréchet derivative of $\mathcal{F}_{k,\boldsymbol{\theta}}^{(V)}$ with respect to the function q
$\mathcal{J}_{k,\boldsymbol{\theta}}^{(T)}$	Fréchet derivative of $\mathcal{F}_{k,\boldsymbol{\theta}}^{(T)}$ with respect to the boundary Γ
\mathcal{S}	single layer potential
\mathcal{D}	double layer potential
\mathcal{K}	normal derivative of the single layer potential
\mathcal{T}	normal derivative of the double layer potential
G	free space Green's function for the two dimensional Helmholtz equation
$N_{\gamma,k}$	number of Fourier modes used to update the curve Γ at wavenumber k
N_m	number of modes in sine series used to update the function q

some indices and write, for example, $\mathcal{F}_k^{(V)}(q) := [\mathcal{F}_{k,\boldsymbol{\theta}_1}^{(V)}(q); \dots; \mathcal{F}_{k,\boldsymbol{\theta}_{N_d}}^{(V)}(q)]$ or \mathbf{u}^{meas} to refer to the vector whose m th component is $\mathbf{u}_{k,\boldsymbol{\theta}}^{meas}(\mathbf{r}_m)$ for incident direction $\boldsymbol{\theta}$ at wavenumber k .

2 Inverse penetrable obstacle scattering

In this section, we first describe an integral equation approach to solving the forward problem (under the assumption that $\rho_i = \rho_e$). We then review the recursive linearization method for the inverse problem (shape recovery) using multifrequency data. The forward transmission scattering operator, defined in the introduction, generates the data vector $\mathbf{u}_{k,\boldsymbol{\theta}}^{meas} = (u_e(\mathbf{r}_1), u_e(\mathbf{r}_2), \dots, u_e(\mathbf{r}_{N_r}))$ for an incident plane wave $u_{k,\boldsymbol{\theta}}^{inc} = e^{ik\mathbf{x}\cdot\boldsymbol{\theta}}$. This requires solving problem (1), for which we use potential theory. We represent the exterior and interior fields as $u_e = (\mathcal{D}_k\sigma - \mathcal{S}_k\mu)$ and $u_i = (\mathcal{D}_{k_i}\sigma - \mathcal{S}_{k_i}\mu)$, where

$$\mathcal{D}_k\sigma = \int_{\Gamma} \frac{\partial G(k\|\mathbf{x} - \mathbf{y}\|)}{\partial\nu(y)} \sigma(\mathbf{y}) ds(y), \quad \text{and} \quad \mathcal{S}_k\mu = \int_{\Gamma} G(k\|\mathbf{x} - \mathbf{y}\|) \mu(\mathbf{y}) ds(y), \quad (7)$$

are the single and double-layer potentials for the domain with wavenumber k . Here, $G(kr) = H_0^{(1)}(kr)$ is the Green's function for the two dimensional Helmholtz equation in free-space, where $H_0^{(1)}$ denotes the first kind Hankel function of order zero satisfying the Sommerfeld radiation condition at infinity. Enforcing the interface conditions on Γ leads to the system of linear integral equations

$$\begin{aligned} [\mathcal{I} + (\mathcal{D}_k - \mathcal{D}_{k_i})] \sigma + (\mathcal{S}_{k_i} - \mathcal{S}_k) \mu &= -u^{inc} \\ (\mathcal{D}'_k - \mathcal{D}'_{k_i}) \sigma + (\mathcal{I} + \mathcal{S}'_{k_i} - \mathcal{S}'_k) \mu &= -\frac{\partial u^{inc}}{\partial \nu}, \end{aligned} \quad (8)$$

where \mathcal{I} is the identity operator, \mathcal{D}'_k and \mathcal{S}'_k are the normal derivatives of the operators \mathcal{D}_k and \mathcal{S}_k and all operators in (8) are interpreted in a principal value sense.

The system above is a Fredholm integral equation of the second kind for the unknown densities (σ, μ) . It is well-known to have a unique solution [30]. For numerical purposes, we discretize the boundary at equispaced points along Γ , using Alpert's 16th order Gauss-trapezoidal rule [1] for quadrature. To ensure more than 10 digits of accuracy, it suffices to use 10 points per wavelength or more, with the wavelength taken to correspond to the larger of the two wavenumbers k_i and k . In all our examples, we used 70 points per wavelength, unless stated otherwise. For simplicity, we solve the resulting system of equations using standard LU factorization, so that the complexity of solution is of the order $\mathcal{O}(N^3)$, where N is the total number of points along the boundary. If N were larger than in the examples considered here, one could replace Gaussian elimination with a fast direct solver that has $\mathcal{O}(N \log N)$ complexity [13, 19, 20, 22, 24, 36, 38, 42, 49]. That approach is discussed for large-scale inverse scattering problems with sound-soft obstacles in [16].

2.1 Inverse obstacle scattering

To recover the shape of the boundary of Γ , we now consider the optimization problem (4). To avoid the expense and complexity of the full multifrequency problem, as noted earlier, we solve a sequence of single frequency problems using recursive linearization [25, 26]. Thus, at each stage, corresponding to exterior wavenumber k_m , we must solve the nonlinear, nonconvex, ill-posed problem

$$\tilde{\Gamma} = \arg \min_{\Gamma} \sum_{\theta_j=1}^{N_d} \|\mathbf{u}_{k_m, \theta_j}^{meas} - \mathcal{F}_{k_m, \theta_j}^{(T)}(\Gamma)\|. \quad (9)$$

Assuming that we have solved the problem correctly at frequency k_{m-1} , the obtained approximation $\Gamma^{(m-1)}$ to Γ should provide a good initial guess for the unknown curve $\Gamma^{(m)}$. That is, we are using frequency as a homotopy parameter, typically using steepest descent or Gauss-Newton iteration to solve for the update $\delta\Gamma^{(m)} = \Gamma^{(m)} - \Gamma^{(m-1)}$. For sufficiently small steps in frequency, this overcomes the intrinsic nonconvexity of (9) (although without a guarantee of global convergence). To address the ill-posedness of the problem, as we march in frequency, we gradually increase the complexity of the curve, parameterized in arclength.

More concretely, at the first stage, using the lowest frequency k_0 , and with no prior information about the curve, we let our initial guess be the unit disk and seek a perturbation $h_1(t)$ in the normal direction to better fit the data. That is, we write

$$\Gamma^{(0)}(t) = e^{it}, \quad h_1(t) = \alpha_0 + \alpha_1 \cos(t) + \beta_1 \sin(t), \quad \delta\Gamma^{(1)}(t) \equiv h_1(t)\boldsymbol{\nu}^{(0)}(t).$$

for $t \in [0, 2\pi]$, With a slight abuse of notation, we make use of the equivalence of \mathbb{R}^2 and the complex plane, and view $\Gamma^{(0)}(t)$ as a complex-valued function whose real and imaginary parts are the x and y components of the curve. The vector $\boldsymbol{\nu}^{(0)}(t)$ denotes the outward normal to $\Gamma^{(0)}(t)$, also treated as a vector in the complex plane. Ignoring for the moment how we actually find $h_1(t)$, we define $\Gamma^{(1)}(t) = \Gamma^{(0)}(t) + \delta\Gamma^{(1)}(t)$ and determine its arclength L_1 . We then reparametrize the curve as

$$\Gamma^{(1)}(t) = \sum_{n=-N_{\gamma,k_1}}^{N_{\gamma,k_1}} \gamma_n^{(1)} e^{2\pi i n t / L_1}.$$

Here, $N_{\gamma,k_1} = \max(1, \frac{pL_1 k_1}{2\pi})$, where p denotes the desired number of points per wavelength (which is typically in the range 10 to 70, as noted above). The general step follows naturally. Since we may do more than one iteration at some wavenumber k_m , let us denote by j the iteration number, by $\Gamma^{(j-1)}(t)$ the previous approximation to the curve with normal $\boldsymbol{\nu}^{(j-1)}(t)$, and by

$$h_j(t) = \alpha_0^{(j)} + \sum_{n=1}^{\lceil ck_m \rceil} \alpha_n^{(j)} \cos(2\pi n t / L_{j-1}) + \beta_n^{(j)} \sin(2\pi n t / L_{j-1}) \quad (10)$$

the newly computed perturbation in the normal direction (by a method to be discussed shortly). We typically choose $c = 2$ and recommend keeping $c \in [1, 3]$. After obtaining the new arclength L_j , one sets

$$\delta\Gamma^{(j)}(t) = h_j(t) \boldsymbol{\nu}^{(j-1)}(t),$$

and reparametrizes the curve as a Fourier series in arclength as

$$\Gamma^{(j)}(t) = \Gamma^{(j-1)}(t) + \delta\Gamma^{(j)}(t) \approx \sum_{n=-N_{\gamma,k_m}}^{N_{\gamma,k_m}} \gamma_n^{(j)} e^{2\pi i n t / L_j}, \quad (11)$$

where

$$N_{\gamma,k_m} = \max(N_{\gamma,k_{m-1}}, \frac{pL_j k_m}{2\pi}). \quad (12)$$

To further stabilize our nonlinear search, we augment the unconstrained formulation (9) with a trust region. For this, with Γ a smooth curve of length L with curvature

$$\kappa(t) = \sum_{n=-\infty}^{\infty} \kappa_n e^{2\pi i n t / L},$$

we define

$$\mathcal{E}_\kappa \equiv \sum_{n=-\infty}^{\infty} |\kappa_n|^2, \quad \mathcal{E}_\kappa^M \equiv \sum_{n=-M}^M |\kappa_n|^2.$$

We will refer to \mathcal{E}_κ as the elastic energy in the curve and \mathcal{E}_κ^M as the elastic energy of its band-limited approximation. We define the set of allowed (closed, non-self-intersecting) curves at wavenumber k (and parameter c) by

$$\mathcal{A}_{k,\epsilon_f} = \{\Gamma \mid \mathcal{E}_\kappa^{\lceil ck \rceil} \geq (1 - \epsilon_f) \mathcal{E}_\kappa\}, \quad (13)$$

i.e., \mathcal{A} is the set of simple closed curves at wavenumber k whose bandlimited approximation captures the bulk $(1 - \epsilon_f)$ of the elastic energy of the curve.

Remark 2.1. Keeping the number of degrees of freedom in $h_j(t)$ and $\Gamma^{(j)}(t)$ proportional to k_m as one increases the incident frequency, and restricting the elastic energy of the curve to nearly bandlimited are forms of regularizations. This mitigates the ill-posedness of (9) in a physically sensible manner, since the signature of high frequency features of the geometry (those that exceed the frequency of the incident wave) decay exponentially in the far field (the Heisenberg uncertainty principle for waves). Attempting to recover those features is unstable.

We return now to the optimization problem itself and write the linearization of the system

$$\mathcal{F}_{k,\theta_j}^{(T)}(\Gamma^{(j-1)} + \delta\Gamma^{(j)}) = \mathbf{u}_{k,\theta_j}^{meas} \quad (14)$$

as

$$\mathcal{J}_{k,\theta_j}^{(T)} \delta\Gamma^{(j)} = \mathbf{u}_{k,\theta_j}^{meas} - \mathcal{F}_{k,\theta_j}^{(T)}(\Gamma^{(j-1)}), \quad (15)$$

where $\mathcal{J}_{k,\theta_j}^{(T)}$ is the Fréchet derivative of the operator $\mathcal{F}_{k,\theta_j}^{(T)}$ for the current guess $\Gamma^{(j-1)}$. For a single angle of incidence, this is an underdetermined system. Using all incident angles, we have the nonlinear least squares problem

$$\mathcal{J}_k^{(T)} \delta\Gamma = \mathbf{u}_k^{meas} - \mathcal{F}_k^{(T)}(\Gamma^{(j-1)}), \quad (16)$$

where

$$\begin{aligned} \mathcal{J}_k^{(T)} &= \left(\mathcal{J}_{k,\theta_1}^{(T)}; \dots; \mathcal{J}_{k,\theta_{N_d}}^{(T)} \right), \\ \mathbf{u}_k^{meas} &= \left(\mathbf{u}_{k,\theta_1}^{meas}; \dots; \mathbf{u}_{k,\theta_{N_d}}^{meas} \right), \\ \mathcal{F}_k^{(T)}(\Gamma^{(j-1)}) &= \left(\mathcal{F}_{k,\theta_1}^{(T)}(\Gamma^{(j-1)}); \dots; \mathcal{F}_{k,\theta_{N_d}}^{(T)}(\Gamma^{(j-1)}) \right). \end{aligned}$$

Following the discussion of [52, 51], the Gauss-Newton solution to (16) is given by

$$\delta\Gamma_{GN} = \left((\mathcal{J}_k^{(T)})^* \mathcal{J}_k^{(T)} \right)^{-1} (\mathcal{J}_k^{(T)})^* \left(\mathbf{u}_k^{meas} - \mathcal{F}_k^{(T)}(\Gamma^{(j-1)}) \right) \quad (17)$$

and the steepest descent direction by

$$\delta\Gamma_{SD} = \left(\mathcal{J}_k^{(T)} \right)^* \left(\mathbf{u}_k^{meas} - \mathcal{F}_k^{(T)}(\Gamma^{(i)}) \right). \quad (18)$$

Rather than use the Gauss-Newton solution in an unconstrained fashion, as in [16, 18], we modify Powell's dogleg method [52, 51], which makes use of a trust region and both the Gauss-Newton and steepest descent steps. In our proposed method, we first calculate $\delta\Gamma_{GN}$ and $\delta\Gamma_{SD}$. We then define $\Gamma_{GN}^{(j)} = \Gamma^{(j-1)} + \delta\Gamma_{GN}$ and $\Gamma_{SD}^{(j)} = \Gamma^{(j-1)} + \delta\Gamma_{SD}$ and check the elastic energies $\mathcal{E}_\kappa, \mathcal{E}_\kappa^{(ck)}$ of the two curves to determine if they lie in the trust region $\mathcal{A}_{k,\epsilon_f}$. We proceed as follows:

- If both curves lie in the trust region, we calculate the residual $\sum_{\theta_j=1}^{N_d} \|\mathcal{F}_{k,\theta_j}^{(T)}(\Gamma) - \mathbf{u}_{k,\theta_j}^{meas}\|$ for both $\Gamma_{GN}^{(j)}$ and $\Gamma_{SD}^{(j)}$ and choose the step with the smaller residual.
- If only one of the updated curves lies in the trust region, we accept that step.

- If neither curve lies in the trust region, we apply a Gaussian filter to the update $\delta\Gamma$. If one or both of the filtered curves $\Gamma_{GN}^{(j)}$ and $\Gamma_{SD}^{(j)}$ lie in the trust region, we continue as above. Otherwise, we repeat the filtering up to 10 times. The Gaussian filter is defined by

$$\gamma_n^{(j)} \rightarrow \gamma_n^{(j)} \exp^{-\frac{n^2}{\sigma^2 N_{\gamma, k_m}^2}}, \quad (19)$$

where $\gamma_n^{(j)}$ are the coefficients defining the update $\delta\Gamma$, and $\sigma = 1/10^{(\ell-1)}$, where ℓ is the iteration number for the filtering step.

Remark 2.2. *The filtering step here is consistent with the discussion in Remark 2.1. If the elastic energy of the curve is not captured by the first N_{γ, k_m} modes, it must have a nontrivial evanescent far-field signature and we are seeking the most band-limited curve that accurately reproduces the measurements. Thus, filtering is consistent with our search regularization strategy. See [17, 18] for further discussion of this point and a more complete description of the algorithm.*

Finally, we conclude this section with a theorem that explains how one actually computes the Fréchet derivative $\mathcal{J}_{k, \theta_j}^{(T)}$ of the operator $\mathcal{F}_{k, \theta_j}^{(T)}$ for a given curve Γ . More precisely, we state how to compute the action of $\mathcal{J}_{k, \theta_j}^{(T)}$ on a normal perturbation $h(t)\boldsymbol{\nu}(t)$. The proof follows very closely that presented in [41, 44].

Theorem 2.1. *Assume that u_i and u_e are the solutions to the transmission problem (1), with incoming field $u^{\text{inc}}(\mathbf{x}) = e^{ik\mathbf{x}\cdot\boldsymbol{\theta}}$, and let $\delta\Gamma = h(s)\boldsymbol{\nu}(s)$ denote a perturbation to the smooth curve Γ in the normal direction. Then, the operator $\mathcal{F}_{k, \theta}^{(T)}$ is Fréchet differentiable at Γ , and the product of its Jacobian with a normal perturbation $\delta\Gamma$, $\mathcal{J}_{k, \theta}^{(T)} \delta\Gamma$, is given at the receiver locations by the solution to the following boundary value problem:*

$$\begin{cases} \Delta v_i + k_i^2 v_i = 0, & \text{in } \Omega_i, \\ \Delta v_e + k^2 v_e = 0, & \text{in } \Omega_e, \\ v_{i-} - v_{e+} = h \left(\frac{\partial u_+}{\partial \nu} - \frac{\partial u_{i-}}{\partial \nu} \right), & \text{on } \Gamma, \\ \frac{\partial v_{i-}}{\partial \nu} - \rho \frac{\partial v_{e+}}{\partial \nu} = \frac{d}{ds} \left(h(s) \frac{d}{ds} (u_{i-} - \rho u_+) \right) + h(s) (k_i^2 u_{i-} - k^2 \rho u_+), & \text{on } \Gamma, \\ \lim_{\|\mathbf{x}\| \rightarrow \infty} \|\mathbf{x}\|^{1/2} \left(\frac{\partial v_e}{\partial r} - ikv_e \right) = 0. \end{cases} \quad (20)$$

In the present paper, after discretizing the curve at $N = 70Lk/(2\pi)$ points, where L is the length of Γ , we apply the preceding theorem to each mode in the expansion of the perturbation $h(s)$, to obtain the columns of the discretized version of $\mathcal{J}_{k, \theta}^{(T)} \delta\Gamma$. From this, we compute $(\mathcal{J}_k^{(T)})^*$ and the steps $\Gamma_{GN}^{(j)}$ and $\Gamma_{SD}^{(j)}$.

To summarize, the recursive linearization algorithm proceeds as outlined above, going from low to high frequency. We refer the reader to [17, 18] for a more detailed discussion of obstacle scattering and also of the “energy landscape” as a function of frequency. It is shown there, empirically, that the higher the frequency, the narrower the basin of attraction for the nonlinear iteration and the more important it is to have a good initial guess. The various parameters introduced here ($N_{\gamma, k}$, ϵ_f) are all aimed at regularizing this process in order to obtain the best, bandlimited approximation of the unknown curve.

3 The inverse medium problem

In this section, we briefly review the inverse medium solver of [15], beginning with a summary of the method used for solving the forward problem (2) to obtain the operator (5).

Since we will be solving the same partial differential equation with many angles of incidence, it is most efficient to use a fast direct solver. There have been a number of such methods proposed over the last decade (see, for example, [2, 3, 19, 20, 23, 27, 32, 33, 40, 42, 48, 57, 58, 37]). In two dimensions (and at high frequency), most of these schemes require $\mathcal{O}(N^{3/2})$ work to factor the relevant linear system, where N denotes the total number of degrees of freedom in the discretization. After factorization, the cost scales linearly with N for each new incident direction (which defines the right-hand side in (2)). As in [15], we have chosen to use the Hierarchical Poincaré-Steklov (HPS) method of [35], since it is both high order accurate and efficient (that is, the constant implicit in the $\mathcal{O}(N)$ notation is small).

The method begins by covering the domain Ω with a quad-tree data structure, designed to resolve $q(x)$ and to ensure a sufficient number of points per wavelength in the discretization. In each leaf node of the tree, a 16×16 grid of Chebyshev nodes is used to sample $q(x)$ and to discretize u^{scat} . Loosely speaking, the HPS method consists of three steps:

- construct solution operators on leaf nodes,
- merge solution operators on leaf nodes to construct solution operators on their “parent” boxes.
- Continue this process recursively until the solution operator for the entire domain is available.

The actual algorithm is more complicated, and involves both an upward pass from the finest level to the root node (a single box containing Ω) and a downward pass from the root node back to the finest level. Since the method is now well established and we use it in its standard form, we leave a detailed description to the original paper [35].

3.1 Regularization and recursive linearization

We turn now to the inverse problem (6), and first consider the single frequency version:

$$\tilde{q} = \arg \min_q \sum_{j=1}^{N_d} \|\mathbf{u}_{k,\theta_j}^{meas} - \mathcal{F}_{k,\theta_j}^{(V)}(q)\|. \quad (21)$$

As with the inverse obstacle problem, (21) is nonlinear, nonconvex, and ill-posed (without some sort of regularization). We will make use of the solver developed in [15] which relies on the Gauss-Newton method as a nonlinear iteration. Given a guess $q^{(j-1)}$, for $j = 1, 2, \dots$, we update the solution by letting $q^{(j)} = q^{(j-1)} + \delta q$ and linearize the forward volumetric scattering operator (5) to obtain the least squares problem

$$\mathcal{J}_k^{(V)} \delta q = \mathbf{u}_k^{meas} - \mathcal{F}_k^{(V)}(q^{(j-1)}), \quad (22)$$

where $\mathcal{J}_k^{(V)} = (\mathcal{J}_{k,\theta_1}^{(V)}; \dots; \mathcal{J}_{k,\theta_{N_d}}^{(V)})$, $\mathcal{F}_k^{(V)} = (\mathcal{F}_{k,\theta_1}^{(V)}; \dots; \mathcal{F}_{k,\theta_{N_d}}^{(V)})$, and $\mathcal{J}_{k,\theta}^{(V)}$ is the Fréchet derivative of $\mathcal{F}_{k,\theta}^{(V)}$.

The following theorem shows that the action of $\mathcal{J}_{k,\theta}^{(T)}$ on a *known* perturbation δq can be obtained by solving a modified scattering problem.

Theorem 3.1. ([15, 31]) Let $u_{k,\theta} = u_{k,\theta}^{\text{inc}} + u_{k,\theta}^{\text{scat}}$ denote the total field obtained by solving the volumetric scattering problem (2), where $u^{\text{inc}}(\mathbf{x}) = e^{ik\mathbf{x}\cdot\boldsymbol{\theta}}$. Then the forward scattering operator $\mathcal{F}_{k,\theta}^{(V)}(q)$ is Fréchet differentiable. Denoting by $J_{k,\theta}^{(V)}$ the Fréchet derivative of $\mathcal{F}_{k,\theta}^{(V)}(q)$, let δq be a given perturbation of the background $q(x)$. Then the product $J_{k,\theta}^{(V)}\delta q$ is given by the solution v to the following PDE evaluated at the receiver locations:

$$\begin{cases} \Delta v + k^2(1+q)v = -k^2\delta q u_{k,\theta}, & \text{in } \mathbb{R}^2 \\ \lim_{\|\mathbf{x}\|\rightarrow\infty} \|\mathbf{x}\|^{1/2} \left(\frac{\partial v}{\partial r} - ikv \right) = 0. \end{cases} \quad (23)$$

The adjoint operator $(J_{k,\theta}^{(V)})^*$ can be applied to a function defined at the receiver locations in a similar fashion.

Theorem 3.2. ([15]) Let $f(\psi)$ denote a smooth function on the circle C of radius R where the sensors are located and let $\xi(f, C)$ denote the corresponding singular charge distribution on C with charge density f , viewed as a generalized function in the plane. Let $\boldsymbol{\theta}$ denote the angle of incidence of an incoming field $u_{k,\theta}^{\text{inc}}$ and let q_0 denote a known inhomogeneity in Ω . Then the product $(J_{k,\theta}^{(V)})^* f$ is given by

$$(J_{k,\theta}^{(V)})^* f = \overline{u_{k,\theta}} w,$$

where $u_{k,\theta}$ denotes the total field satisfying (2) with $q = q_0$, and w satisfies

$$\begin{cases} \Delta w + k^2(1+q_0)w = -k^2\xi(f, C), & \text{in } \mathbb{R}^2 \\ \lim_{\|\mathbf{x}\|\rightarrow\infty} \|\mathbf{x}\|^{1/2} \left(\frac{\partial w}{\partial r} - ikw \right) = 0. \end{cases} \quad (24)$$

The preceding theorems permit the solution of the (22) iteratively, using conjugate gradient iteration on the normal equations or LSQR iteration [50, 12], rather than with a direct solver as in (17). The number of such steps (indexed by j in equation (22)) is controlled by a stopping criterion. We halt when either (a) the total number of allowed iterations N_{it} has been reached, (b) the value of the relative residual $\|\mathbf{u}^{\text{meas}} - \mathcal{F}_k^{(V)}(q^{(j)})\|/\|\mathbf{u}^{\text{meas}}\| < \epsilon_{res}$, (c) the relative size of the update $\|\delta q\|/\|q\| < \epsilon_{\delta q}$, or (d) the residual has increased on the last step.

Recursive linearization [25, 26] is applied to the inverse medium problem in the same manner as for the obstacle scattering problem, following the method described in greater detail in [15]. We march from low to high frequency, with the solution obtained at frequency k_m used as the initial guess for the solution at frequency k_{m+1} . By itself, this is not sufficient to overcome the ill-posedness of the inverse medium problem. At a given frequency, as discussed above, the far field signature of features that are subwavelength in size is exponentially decaying (the Heisenberg Principle for waves). Thus, we bandlimit both $q(x, y)$ and the update $\delta q(x, y)$ using the representation

$$\begin{bmatrix} q(x, y) \\ \delta q(x, y) \end{bmatrix} = \begin{cases} \sum_{\substack{m,n=1 \\ m+n \leq N_m}}^{N_m} \begin{bmatrix} q_{m,n} \\ \delta q_{m,n} \end{bmatrix} \sin(m(x + \pi/2)) \sin(n(y + \pi/2)), & (x, y) \in [-\pi/2, \pi/2]^2, \\ 0, & (x, y) \notin [-\pi/2, \pi/2]^2, \end{cases} \quad (25)$$

where N_m is an integer multiple of the wavenumber k_m . This imposes both compact support and regularizes the inverse problem, controlling the condition number of the linear least squares problem to be solved at each frequency.

Remark 3.1. *At low frequencies, one can simply build the discrete version of $J_{k,\theta}^{(V)}$ in the sine series basis and solve the least squares problem directly (using QR factorization). At higher frequencies, we switch to an iterative method such as conjugate gradient on the normal equations or LSQR, as noted above.*

4 Numerical results

The stability and effectiveness of recursive linearization within the inverse obstacle solver and the inverse medium solver are sensitive to the amount of measured data available at each frequency, the contrast of the problem k^2/k_i^2 , and the complexity of the domain. In this section, we explore the impact of these parameters through several numerical examples.

For each example, unless stated otherwise, we assume that scattered field measurements are made for M frequencies, $k_\ell = 1 + (\ell - 1)\delta k$, $\ell = 1, 2, \dots, M$, with $\delta k = 0.25$, $M = 117$, so that $k = 30$ is the maximum frequency for which data is available. For each frequency, the data is obtained by solving the transmission problem where the obstacle is discretized with 100 points per wavelength. Scattered field measurements are made for N_d incident waves and at N_r receiver locations for each incident wave, with equispaced angles of incidence $\theta_j = (\cos(2\pi j/N_d), \sin(2\pi j/N_d))$, $j = 1, 2, \dots, N_d$, and equispaced receiver locations $r_m = 10(\cos(2\pi m/N_r), \sin(2\pi m/N_r))$. For most examples, we assume $N_d = N_r = \lfloor 10k \rfloor$ at wavenumber k so as to ensure that the measured data is resolved as a function of both the incidence angle and the spacing of the receiver locations. Obtaining such highly-resolved full aperture data tends to be difficult in practice. However, this idealized environment makes it feasible to study the sensitivity of the inverse solvers with respect to the contrast and complexity of the domain without a simultaneous concern about the resolution of the scattered field measurements.

For the inverse obstacle solver, the update at frequency k is represented by the trigonometric series (10) with $N_\gamma = \lfloor 3 \max(k, k_i) \rfloor$ modes, while the update δq for the inverse medium solver is parameterized by a sine series (25) with bandlimit $N_m = \lfloor 2k \rfloor$. The stopping criteria for both the inverse solvers were based on three considerations – maximum number of iterations $n_{\max\text{-iter}}$, size of the relative residual ε_r , and the size of the update $\varepsilon_u = \|\delta\bar{\gamma}\|_2$ for the obstacle problem, and $\varepsilon_u = \|\delta\bar{q}\|_2/\|q\|_2$ for the medium problem. Note that we use the relative size of the update for the volume solver to account for the fact that the contrast is unknown for the inverse medium problem. For the inverse obstacle problem, we use $\varepsilon_r = \varepsilon_u = 10^{-5}$, and $n_{\max\text{-iter}} = 50$, while for the inverse medium problem, we use $\varepsilon_r = \varepsilon_u = 10^{-3}$, and $n_{\max\text{-iter}} = 50$. The stopping criteria have been chosen to ensure that the final reconstructions using both the solvers have converged and are not impacted by the specific choices made.

We estimate the error in the reconstruction obtained using the inverse obstacle solver by an estimate of the earth mover’s distance. For this, suppose that the true obstacle boundary, and the reconstructed curve are approximated by a polygon. Let δA denote the area of the set difference between these two polygons, and let A denote the area of the true obstacle boundary. Then, $\varepsilon_\Gamma = \delta A/A$ is used as a measure of the relative error for the inverse obstacle problem. For the inverse medium problem, if q denotes the true medium, then $\varepsilon_q = \|q_r(k) - q\|_2/\|q\|_2$ is the relative L^2 error in the reconstruction of the medium, where $q_r(k)$ is the reconstructed medium at frequency k . We also compare ε_q to the relative error of the best approximation of q in the bandlimited basis given by $\varepsilon_{q_b} = \|q_b(k) - q\|_2/\|q\|_2$, where $q_b(k)$ is the best approximation (in an L^2 sense) to q in the sine basis with bandlimit N_m .

Each of the examples below is intended to highlight a specific feature of the inverse problem, ordered as in Table 2.

Example	Description	Figures
1	Impact of contrast	1-3
2	Effect of using limited data	4-6
3	Reconstruction of a trapping domain	7,8
4	Reconstruction of an obstacle with multiple components	9

Table 2: List of numerical examples with respective results.

4.1 Contrast

In this section, we explore the impact of the contrast, $\eta = k_i^2/k^2$ on the reconstructions obtained using the inverse obstacle and the inverse medium solvers. Consider the reconstruction of a star shaped “glider” using the inverse obstacle solver with $\eta = 0.33$ and $\eta = 10$. The boundary of the glider is parameterized by $\gamma : [0, 2\pi] \rightarrow \mathbb{R}^2$ with $\gamma(t) = r(t)(\cos(t), \sin(t))$, where $r(t) = 0.9(1 + \sum_{j=1}^8 c_j \cos(jt))$, with $c_3 = 0.2$, $c_4 = 0.02$, $c_6 = 0.1$, $c_8 = 0.1$, and $c_j = 0$, for all other values of j . In Figure 1, we plot the reconstructions at $k = 1, 5$, and 10. We also plot the error $\varepsilon_{\Gamma}(k)$ corresponding to the reconstruction at wavenumber k . The contrast of the object does not seem to have a significant impact on the quality of the reconstruction, and the shape of the obstacle can be recovered in a robust manner independent of the contrast of the problem.

For the inverse medium solver, it is well known that the problem becomes easier as $\eta \rightarrow 1$, where the Born approximation leads to a more and more accurate solution. As we increase η , the problem becomes increasingly nonlinear – and waves interact with the inhomogeneity in more and more complicated ways. Consider the reconstruction of a unit circle centered at $(0.3, 0.3)$ with $\eta = 1.4, 1.5, 1.6$, and 1.7. In Figure 2, we plot the final reconstructions, a cross-section of the reconstruction through the line $(x, 0.3)$, and the relative errors $\varepsilon_q(k)$ and $\varepsilon_{q_b}(k)$ for all four cases. As the contrast is increased, note that the Gibbs oscillations near the boundary of the circle increase in magnitude. Moreover, the relative error ε_q closely follows the relative error for the best reconstruction ε_{q_b} for low contrasts, indicating that the inverse medium solver is optimal in the bandlimited basis. However, as the contrast increases, the relative error ε_q increasingly deviates from ε_{q_b} , and the deviation begins at an earlier frequency for higher values of contrast.

This behavior can be attributed to the failure of the initial guess in the frequency marching process to lie within the basin of attraction of the *best* approximation. More precisely, suppose that when $k \rightarrow k + \delta k$, the bandlimit of the sine series increases by 1, i.e. $N_m \rightarrow N_m + 1$. Following eq. 25, the new coefficients $q_{m,n}$, for $m + n = N_m + 1$ are initialized to 0. The local basin of attraction of the best reconstruction, however, is approximately $O(1/k)$ in size. Since $N_m = O(k)$, for C^1 media, the Fourier coefficients decay faster than $O(1/|N_m|^2) = O(1/k^2)$ as $k \rightarrow \infty$. This implies that an initialization of the new coefficients to 0 at $k + \delta k$ would roughly be $O(1/k^2)$ away from the best reconstruction in the bandlimited basis, and thus would likely remain in the local basin of attraction as we march in frequency. However, when recovering a discontinuous function, as is the case for our penetrable obstacle, the Fourier coefficients of the medium decay as $O(1/k)$ and the initialization to zero could well lie outside the basin of attraction. We can illustrate this

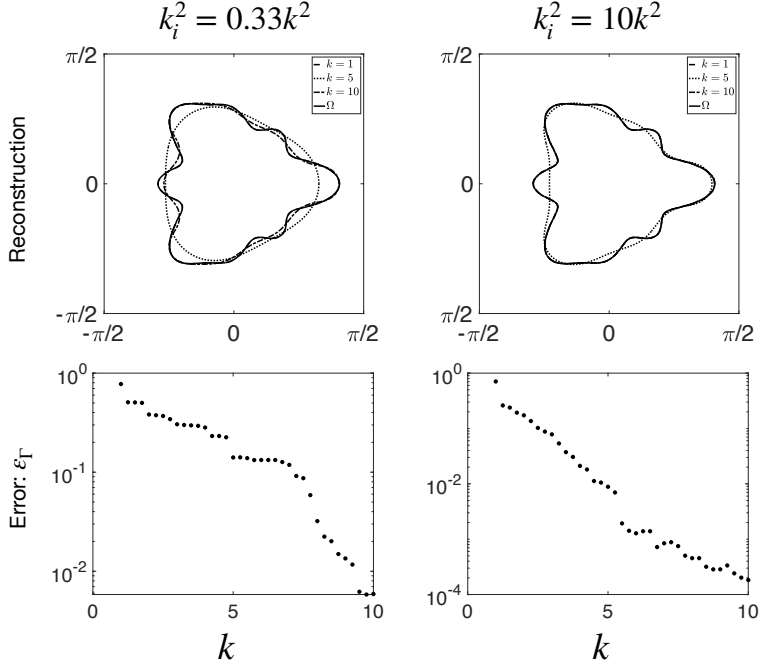


Figure 1: **Effect of contrast on inverse obstacle solver:** Reconstructions of a star-shaped plane using the inverse obstacle solver and the relative error in its reconstruction ϵ_Γ .

with a simple example. Consider the inverse problem with contrast $k_i^2 = 1.7k^2$. Let \mathbf{q}_0 denote the initial guess at $k = 13.5$, and let \mathbf{q}_1 denote the reconstruction obtained at using Gauss-Newton. Let \mathbf{q}_b denote the vector with the coefficients of the best sine series approximating the circle with the same bandlimit as \mathbf{q}_0 , and \mathbf{q}_1 . Let

$$\mathcal{U} = \{\mathbf{q}_0 + c_0(\mathbf{q}_b - \mathbf{q}_0) + c_1(\mathbf{q}_1 - \mathbf{q}_0) | c_0, c_1 \in \mathbb{R}\}. \quad (26)$$

In Figure 3, we plot the objective function $\|\mathcal{F}_k^{(V)}(\mathbf{q}) - u^{meas}\|_{\mathbf{q} \in \mathcal{U}}$ in a neighborhood of \mathbf{q}_0 . The figure shows that the initial guess \mathbf{q}_0 lies outside of the local set of convexity which includes the best solution \mathbf{q}_b , thus the reconstruction obtained using the Gauss-Newton approach ends up deviating from the best solution in the bandlimited basis.

4.2 Effect of limited data

In our next example, we compare the performance of the inverse obstacle and inverse medium solvers on complicated star-shaped domains when the scattered field measurements are not completely resolved as a function of the incidence angle or receiver locations at high frequencies. The (x, y) coordinates describing the boundary of the curve are given by a 35 term Fourier series, i.e.

$$\begin{bmatrix} x(t) \\ y(t) \end{bmatrix} = \sum_{n=-35}^{35} \begin{bmatrix} \hat{x}_n \\ \hat{y}_n \end{bmatrix} e^{int}, \quad t \in [0, 2\pi). \quad (27)$$

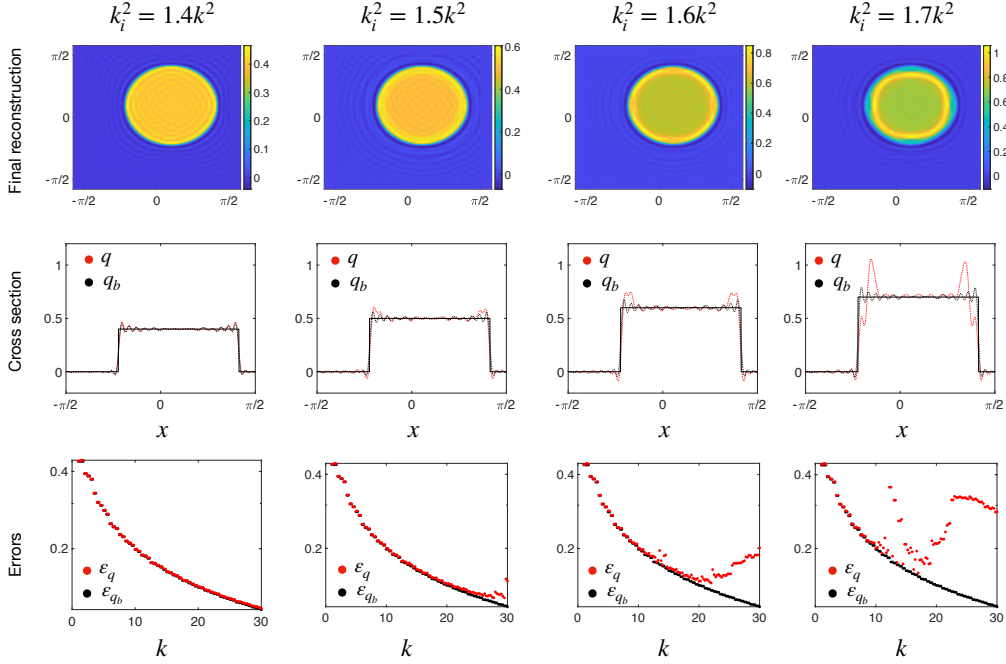


Figure 2: **Effect of contrast on inverse medium solver:** Reconstructions of the circle and its relative error using the inverse medium solver. For each of the contrasts, we present the reconstruction at $k = 30$, the cross section of this reconstruction through the line $(x, 0.3)$, $x \in [-\pi/2, \pi/2]$ and the error of the reconstruction in the the first, second and third rows, respectively.

Measurements are made for $k_i = 0.9k^2$ for two sets of receiver locations and incident fields: one with $(N_r, N_d) = ([10k], [10k])$, and one with $(N_r, N_d) = (200, 10)$. Note that the measurements are still full-aperture, however for the second case, the sensor measurements are not resolved for $k \geq 5$. The contrast is chosen to be low in order to isolate the effect of limited data on the reconstructions.

In Figure 4, we plot the reconstructions obtained using the inverse obstacle solver at $k = 1, 15$, and 30 , and the inverse medium solver at $k = 15$ and 30 , and in Figure 5, we plot the error in reconstruction $\varepsilon_\Gamma(k)$ for the inverse obstacle solver, and the error in reconstruction for the inverse medium solver $\varepsilon_q(k)$, along with the error for the best solution in the bandlimited basis ε_{q_b} . To illustrate the lack of resolution of the measured data, we also plot

$$\tau^{\text{meas}} = \frac{1}{\max_{m,n} |\hat{u}_{m,n}|} \left(\sum_{m=-\frac{N_r}{2}+1}^{\frac{N_r}{2}} (|\hat{u}_{m,-N_d/2+1}| + |\hat{u}_{m,N_d/2}|) + \sum_{n=-\frac{N_d}{2}+1}^{\frac{N_d}{2}} (|\hat{u}_{-N_r/2+1,n}| + |\hat{u}_{N_d/2,n}|) \right), \quad (28)$$

where $\hat{u}_{m,n}$ are the Fourier series coefficients of the measured data, i.e.

$$u^{\text{meas}}(\theta, \phi) = \sum_{m=-\frac{N_r}{2}+1}^{\frac{N_r}{2}} \sum_{n=-\frac{N_d}{2}+1}^{\frac{N_d}{2}} \hat{u}_{m,n} e^{i(m\theta+n\phi)}. \quad (29)$$

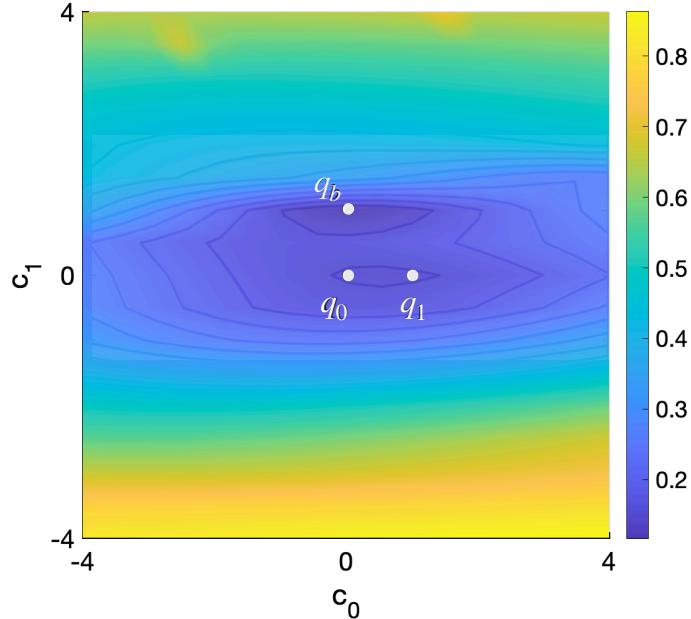


Figure 3: **Inverse medium problem landscape:** Contour plot of the objective function for $k = 13.5$ evaluated at the plane \mathcal{U} (see (26)). \mathbf{q}_0 is the initial guess, \mathbf{q}_1 is the solution obtained using Gauss-Newton, and \mathbf{q}_b is the best solution in the bandlimited basis.

Both the inverse medium solver, and inverse obstacle solver recover the obstacle to high fidelity when sufficient data is available to resolve the scattered field measurements. However, the inverse medium solver deviates from the best solution in the bandlimited basis when the data is insufficient to resolve the scattered field (approximately when $\tau^{\text{meas}} > 0.1$), while the inverse obstacle solver robustly recovers the shape even with unresolved scattered field measurements. The inverse obstacle solver tends to perform better than the inverse medium solver with fewer measurements of the scattered field, since at wavenumber k , the obstacle is described by $O(k)$ parameters while the medium is described by $O(k^2)$ parameters.

Finally, in Figure 6, we plot the number of iterations n_{iter} in the optimization loop at each frequency. It is interesting to note that the inverse medium solver tends to take fewer steps when compared to the inverse obstacle solver. This behavior is independent of the shape of the obstacle being recovered, and can be attributed, perhaps, to the more systematic increase in resolution that is achieved via the tensor-product sine series in the volumetric case. That said, the computational complexity of both of these approaches is comparable, since the obstacle problem benefits from dimensionality reduction: one needs to solve only a boundary integral equation instead of a volumetric Lippmann-Schwinger equation.

4.3 Cavity-like domains

In our next example, we investigate the behavior of the two solvers for (highly nonconvex) cavities, which are challenging; the solutions on such domains tend to have a complicated behavior as a

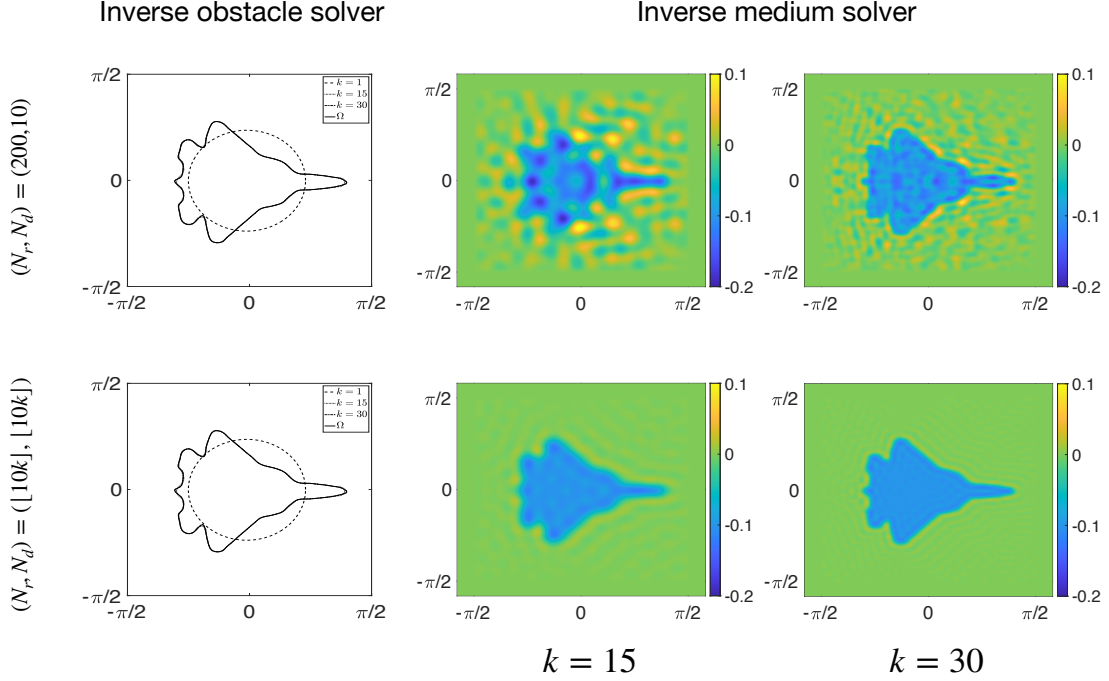


Figure 4: **Reconstructions for the limited data experiment:** Reconstruction of a star-like plane using the inverse obstacle solver at frequencies $k = 1, 15,$ and 30 (left), the inverse medium solver at $k = 15$ (middle), or the inverse medium solver at $k = 30$ (right). The top row results correspond to underresolved scattered field measurements at high frequencies, while the bottom row results correspond to fully resolved scattered field measurements.

function of frequency owing to the wave-trapping nature of the domain. The cavity used for this example is illustrated by the curve in the left-hand panels of Figure 7. In that figure, we plot the reconstructions obtained using the inverse obstacle solver and the inverse medium solver at $k = 15,$ and $k = 30$ for two different contrast values $k_i^2 = 0.9k^2$ and $k_i^2 = 2k^2$. The results show that the inverse obstacle solver is unable to resolve the shape of the domain, while the inverse medium solver performs significantly better. This is further illustrated in Figure 8, where we plot the level set corresponding to $q/2,$ namely $q = -0.05$ in the low contrast case and $q = 0.5$ in the higher contrast case. This is where one would expect the boundary to lie in a truncated Fourier series subject to the Gibbs phenomenon.

4.4 Multiple obstacles

For our final example, we consider the reconstruction of multiple, disjoint scatterers using both the inverse obstacle and inverse medium solvers. The domain consists of three identical star-shaped scatterers with $k_i^2 = 2k^2$ for each (see the left panel of Figure 9). At wavenumber $k,$ measurements are made for $[10k]$ incident directions at $[10k]$ sensor locations. While the inverse medium solver

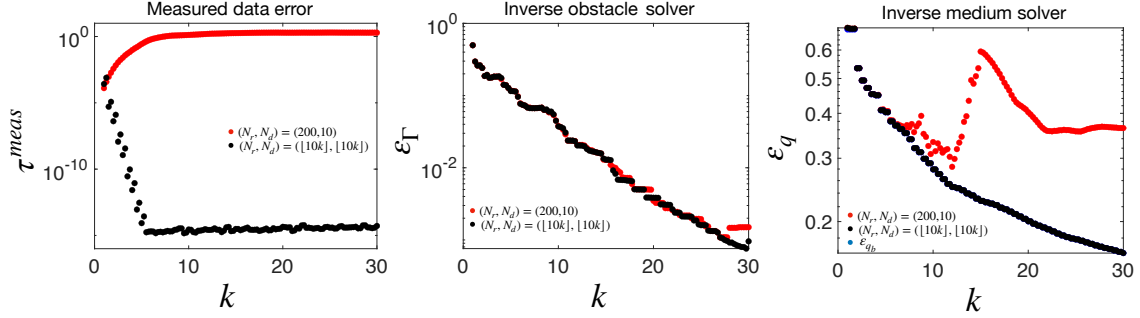


Figure 5: **Errors in reconstruction and measurement data for the limited data experiment:** (left) Resolution of measurement data τ^{meas} , (middle) error in reconstruction for the inverse obstacle solver ε_Γ , and (right) error in reconstruction for the inverse medium solver ε_q along with the error in the best reconstruction in the bandlimited basis ε_{q_b} , all as a function of frequency.

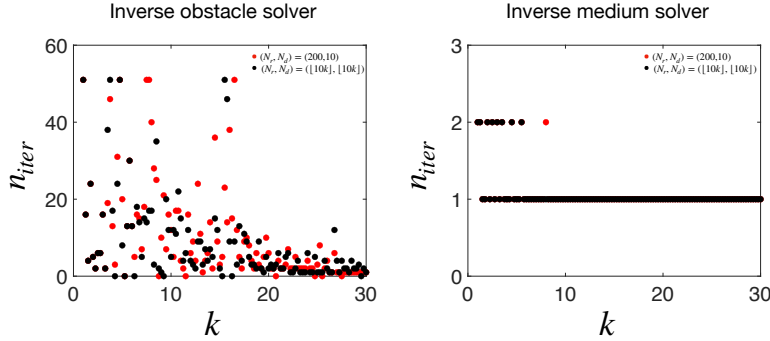


Figure 6: **Iteration count for inverse solvers in limited data experiment:** Number of iterations n_{iter} in the optimization loop at frequency k for the inverse obstacle solver (left), and the inverse medium solver (right).

should not be impacted by the presence of multiple scatterers, this is a challenging problem for the inverse obstacle solver since our model is parametrized as a single closed curve.

In Figure 9, we plot the reconstructions obtained using both solvers at $k = 15$, and $k = 30$. Since the obstacles are separated by more than a wavelength corresponding to the smallest wavelength for which measurements are made, the inverse medium solver is robustly able to recover the boundary of the multiple obstacles. Perhaps surprisingly, the inverse obstacle solver also performs well, and is able to capture the bulk of the boundary accurately, with the three scatterers connected via thin bridges. Detecting such a feature could serve as a signal that multiple obstacles are present, which could be used, in turn, to modify the number of components used in the model.

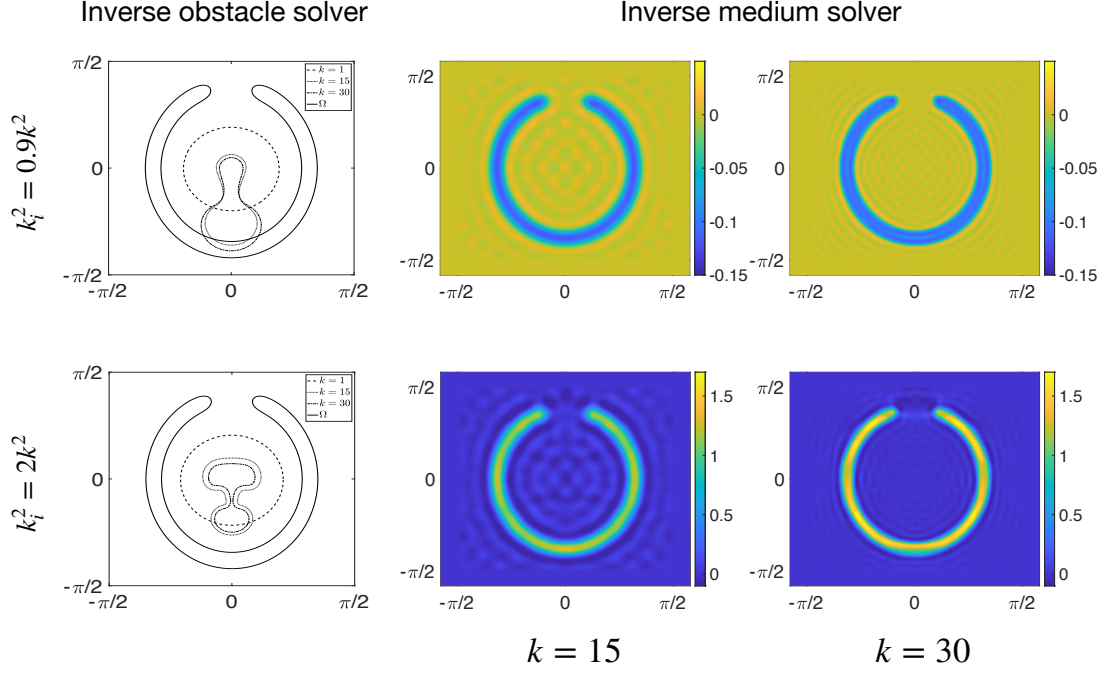


Figure 7: **Reconstructions of a trapping domain:** Reconstruction of a trapping cavity-like domain using the inverse obstacle solver at frequencies $k = 1, 15,$ and $30,$ using the inverse medium solver at $k = 15,$ and using the inverse medium solver at $k = 30,$ in the left, middle and right columns. The top row results are for $k_i^2 = 0.9k^2,$ and the bottom row results correspond to $k_i^2 = 2k^2.$

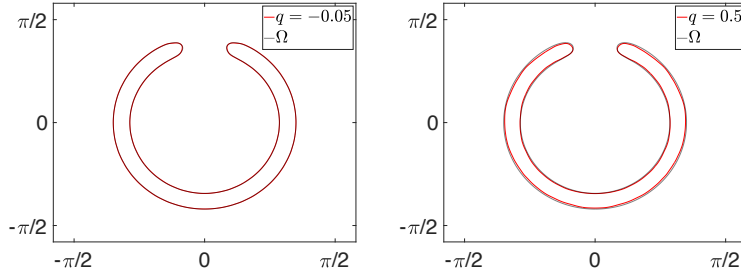


Figure 8: **Level sets from the inverse medium solver for the trapping domain:** (left) level set for $k_i^2 = 0.9k^2,$ and (right) level set for $k_i^2 = 2k^2.$ The boundary of the curve used to generate the data is plotted in gray in both figures.

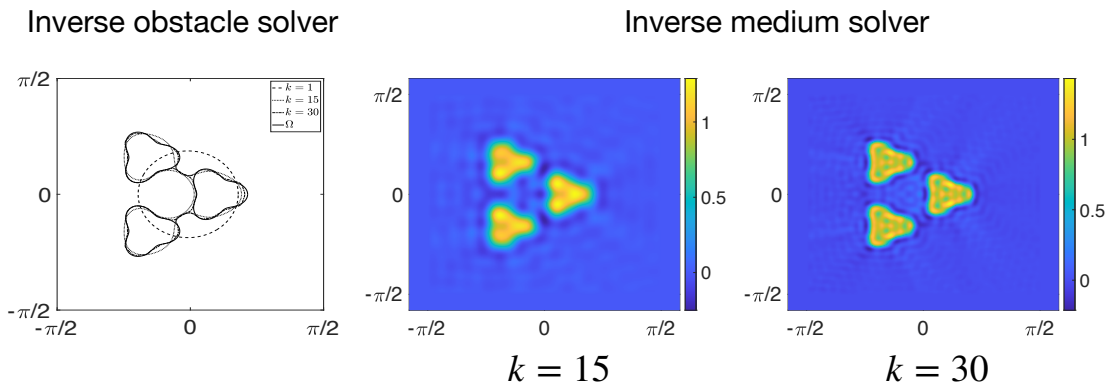


Figure 9: **Reconstructions of multiple scatterers:** Reconstructions of three star shaped scatterers using the inverse obstacle solver at frequencies $k = 1, 15$, and 30 , using the inverse medium solver at $k = 15$, and using the inverse medium solver at $k = 30$, in the left, middle and right columns.

5 Conclusions

In this paper, we compare the performance of an inverse obstacle solver for transmission boundary value problems and an inverse medium solver for the reconstruction of penetrable media. For both solvers, full aperture measurements are made at multiple frequencies, and a recursive linearization based approach is used as a continuation method for solving the a sequence of single frequency optimization problems.

We present several numerical examples which highlight the benefits and disadvantages of the two approaches. The inverse obstacle solver requires the determination of a simple curve, while the inverse medium solver discretizes an entire two dimensional volume. We have found that the inverse obstacle solver tends to perform better when the number of incidence directions and receiver locations are insufficient to resolve the scattered field measurements. This is to be expected, since many fewer degrees of freedom are required for describing the unknown obstacle. On the other hand, the constrained optimization problem for the inverse medium solver appears to be better posed, since the space of compactly supported perturbations comes equipped with a natural basis (such as a sine series), and it is straightforward to systematically increase the bandlimit. For the inverse obstacle problem, the geometry of the set of non-intersecting curves is complicated to parametrize, and constructing a constraint set which appropriately bandlimits the curve poses a significant challenge and local linearization appears to be less robust. The difference in the optimization landscape between these two problems manifests itself in two ways. First, for all obstacles, the inverse medium solver tends to require fewer optimization steps at each frequency. Second, the inverse medium solver is more robust for reconstructing complicated shapes such as cavity-like structures, where the measurement data can vary sharply across frequencies, due to the trapping nature of the domain.

However, the inverse medium solver is more sensitive to contrast, deviating from the best solution in the bandlimited basis as the contrast is increased. This behavior could be due to poor initialization of the Newton iteration as we march in frequency - a question which is currently being

explored.

Given the better stability of the inverse obstacle solver when scattered field measurements are limited, and the better behavior of the inverse medium solver in complicated cavity-like domains, one can imagine using the inverse medium solver at low frequencies to construct a good initial guess and to continue from that point using the inverse obstacle solver at higher frequencies. Such hybrid schemes are under investigation.

Finally, we showed that both solvers were able to handle the case of multiple scatterers. For the inverse medium solver, this is to be expected, since the collection of scatterers is treated together as an unknown function to be recovered. We were surprised that, without prior knowledge of the number of scatterers, the inverse obstacle solver was able to recover the geometry with high fidelity, stitching together the scatterers with very thin bridges. We suspect that the presence of such thin bridges could be used as a monitor to detect the presence of multiple scatterers and the reconstruction could be further refined by adjusting the number of boundary curves during the optimization process. This is also an area of ongoing research.

Acknowledgments

The work of C. Borges was supported in part by the Office of Naval Research under award number N00014-21-1-2389. The authors would like to thank Jeremy Hoskins and Travis Askham for many useful discussions.

References

- [1] B. K. ALPERT, *Hybrid Gauss-Trapezoidal Quadrature Rules*, SIAM Journal on Scientific Computing, 20 (1999), pp. 1551–1584.
- [2] S. AMBIKASARAN, C. BORGES, L.-M. IMBERT-GERARD, AND L. GREENGARD, *Fast, adaptive, high-order accurate discretization of the lippmann-schwinger equation in two dimensions*, SIAM Journal on Scientific Computing, 38 (2016), pp. A1770–A1787.
- [3] S. AMBIKASARAN AND E. DARVE, *An $O(N \log N)$ Fast Direct Solver for Partial Hierarchically Semi-Separable Matrices*, Journal of Scientific Computing, 57 (2013), pp. 477–501.
- [4] G. BAO, S. HOU, AND P. LI, *Inverse scattering by a continuation method with initial guesses from a direct imaging algorithm*, Journal of Computational Physics, 227 (2007), pp. 755–762.
- [5] G. BAO AND P. LI, *Inverse medium scattering problems for electromagnetic waves*, SIAM Journal on Applied Mathematics, 65 (2005), pp. 2049–2066.
- [6] G. BAO, P. LI, J. LIN, AND F. TRIKI, *Inverse scattering problems with multi-frequencies*, Inverse Problems, 31 (2015), p. 093001.
- [7] G. BAO AND J. LIN, *Imaging of local surface displacement on an infinite ground plane: the multiple frequency case*, SIAM Journal on Applied Mathematics, 71 (2011), pp. 1733–1752.
- [8] G. BAO, J. LIN, AND F. TRIKI, *A multi-frequency inverse source problem*, Journal of Differential Equations, 249 (2010), pp. 3443–3465.

- [9] G. BAO, J. LIN, F. TRIKI, ET AL., *Numerical solution of the inverse source problem for the helmholtz equation with multiple frequency data*, Contemp. Math, 548 (2011), pp. 45–60.
- [10] G. BAO, S. LU, W. RUNDELL, AND B. XU, *A recursive algorithm for multifrequency acoustic inverse source problems*, SIAM Journal on Numerical Analysis, 53 (2015), pp. 1608–1628.
- [11] G. BAO AND F. TRIKI, *Error estimates for the recursive linearization of inverse medium problems*, Journal of Computational Mathematics, (2010), pp. 725–744.
- [12] R. BARRETT, M. BERRY, T. F. CHAN, J. DEMMEL, J. DONATO, J. DONGARRA, V. EIJKHOUT, R. POZO, C. ROMINE, AND H. VAN DER VORST, *Templates for the solution of linear systems: building blocks for iterative methods*, SIAM, 1994.
- [13] M. BEBENDORF, *Hierarchical LU decomposition-based preconditioners for BEM*, Computing, 74 (2005), pp. 225–247.
- [14] L. BEILINA, N. T. THANH, M. V. KLIBANOV, AND J. B. MALMBERG, *Reconstruction of shapes and refractive indices from backscattering experimental data using the adaptivity*, Inverse Problems, 30 (2014), p. 105007.
- [15] C. BORGES, A. GILLMAN, AND L. GREENGARD, *High resolution inverse scattering in two dimensions using recursive linearization*, SIAM Journal on Imaging Sciences, 10 (2017), pp. 641–664.
- [16] C. BORGES AND L. GREENGARD, *Inverse Obstacle Scattering in Two Dimensions with Multiple Frequency Data and Multiple Angles of Incidence*, SIAM J. Imaging Sciences, 8 (2015), pp. 280–298.
- [17] C. BORGES AND J. LAI, *Inverse scattering reconstruction of a three dimensional sound-soft axis-symmetric impenetrable object*, Inverse Problems, 36 (2020), p. 105005.
- [18] C. BORGES AND M. RACHH, *Multifrequency inverse obstacle scattering with unknown impedance boundary conditions using recursive linearization*, Advances in Computational Mathematics, 48 (2022), pp. 1–32.
- [19] S. BÖRM, L. GRASEDYCK, AND W. HACKBUSCH, *Hierarchical matrices*, Lecture notes, 21 (2003), p. 2003.
- [20] ———, *Introduction to hierarchical matrices with applications*, Engineering analysis with boundary elements, 27 (2003), pp. 405–422.
- [21] S. CHAILLAT AND G. BIROS, *FaIMS: A fast algorithm for the inverse medium problem with multiple frequencies and multiple sources for the scalar Helmholtz equation*, Journal of Computational Physics, 231 (2012), pp. 4403 – 4421.
- [22] S. CHANDRASEKARAN, P. DEWILDE, M. GU, W. LYONS, AND T. PALS, *A fast solver for HSS representations via sparse matrices*, SIAM Journal on Matrix Analysis and Applications, 29 (2006), pp. 67–81.
- [23] S. CHANDRASEKARAN, P. DEWILDE, M. GU, W. LYONS, AND T. PALS, *A fast solver for hss representations via sparse matrices*, SIAM Journal on Matrix Analysis and Applications, 29 (2007), pp. 67–81.

- [24] S. CHANDRASEKARAN, M. GU, AND T. PALS, *A fast ULV decomposition solver for hierarchically semiseparable representations*, SIAM Journal on Matrix Analysis and Applications, 28 (2006), pp. 603–622.
- [25] Y. CHEN, *Recursive linearization for inverse scattering*, Mathematical and numerical aspects of wave propagation (Golden, CO, 1998), (1995), pp. 114–117.
- [26] Y. CHEN, *Inverse scattering via Heisenberg’s uncertainty principle*, Inverse Problems, 13 (1997), p. 253.
- [27] Y. CHEN, *A fast, direct algorithm for the lippmann–schwinger integral equation in two dimensions*, Advances in Computational Mathematics, 16 (2002), pp. 175–190.
- [28] M. CHENEY AND B. BORDEN, *Fundamentals of Radar Imaging*, CBMS-NSF Regional Conference Series in Applied Mathematics, Society for Industrial and Applied Mathematics, 2009.
- [29] R. COLLINS, *Nondestructive Testing of Materials*, Studies in applied electromagnetics and mechanics, IOS Press, 1995.
- [30] D. COLTON AND R. KRESS, *Integral equation methods in scattering theory*, SIAM, 2013.
- [31] ———, *Inverse Acoustic and Electromagnetic Scattering Theory*, Springer, 4nd ed., 2019.
- [32] E. CORONA, P.-G. MARTINSSON, AND D. ZORIN, *An $\mathcal{O}(n)$ direct solver for integral equations on the plane*, Applied and Computational Harmonic Analysis, 38 (2015), pp. 284–317.
- [33] P. COULIER, H. POURANSARI, AND E. DARVE, *The inverse fast multipole method: using a fast approximate direct solver as a preconditioner for dense linear systems*, SIAM Journal on Scientific Computing, 39 (2017), pp. A761–A796.
- [34] H. ENGL, A. LOUIS, AND W. RUNDELL, *Inverse Problems in Medical Imaging and Nondestructive Testing: Proceedings of the Conference in Oberwolfach, Federal Republic of Germany, February 4–10, 1996*, Springer Vienna, 2012.
- [35] A. GILLMAN, A. H. BARNETT, AND P.-G. MARTINSSON, *A spectrally accurate direct solution technique for frequency-domain scattering problems with variable media*, BIT Numerical Mathematics, 55 (2015), pp. 141–170.
- [36] A. GILLMAN, P. M. YOUNG, AND P. G. MARTINSSON, *A direct solver with $\mathcal{O}(N)$ complexity for integral equations on one-dimensional domains*, Frontiers of Mathematics in China, 7 (2012), pp. 217–247.
- [37] A. GOPAL AND P.-G. MARTINSSON, *An accelerated, high-order accurate direct solver for the lippmann-schwinger equation for acoustic scattering in the plane*, arXiv preprint arXiv:2007.12718, (2020).
- [38] L. GREENGARD, D. GUEYFFIER, P. G. MARTINSSON, AND V. ROKHLIN, *Fast direct solvers for integral equations in complex three-dimensional domains*, Acta Numerica, 18 (2009), pp. 243–275.

- [39] L. GREENGARD AND J.-Y. LEE, *Stable and accurate integral equation methods for scattering problems with multiple material interfaces in two dimensions*, Journal of Computational Physics, 231 (2012), pp. 2389–2395.
- [40] W. HACKBUSCH, L. GRASEDYCK, AND S. BÖRM, *An introduction to hierarchical matrices*, (2001).
- [41] F. HETTLICH, *Fréchet derivatives in inverse obstacle scattering*, Inverse Problems, 11 (1995), p. 371.
- [42] K. L. HO AND L. GREENGARD, *A fast direct solver for structured linear systems by recursive skeletonization*, SIAM Journal on Scientific Computing, 34 (2012), pp. A2507–A2532.
- [43] T. HOHAGE, *Logarithmic convergence rates of the iteratively regularized Gauss - Newton method for an inverse potential and an inverse scattering problem*, Inverse Problems, 13 (1997), pp. 1279–1299.
- [44] T. HOHAGE AND C. SCHORMANN, *A newton-type method for a transmission problem in inverse scattering*, Inverse Problems, 14 (1998), p. 1207.
- [45] M. V. KLIBANOV, A. E. KOLESOV, AND D.-L. NGUYEN, *Converification method for an inverse scattering problem and its performance for experimental backscatter data for buried targets*, SIAM Journal on Imaging Sciences, 12 (2019), pp. 576–603.
- [46] R. KRESS, *Uniqueness and numerical methods in inverse obstacle scattering*, Journal of Physics: Conference Series, 73 (2007), p. 012003.
- [47] P. KUCHMENT, *The Radon Transform and Medical Imaging*, CBMS-NSF Regional Conference Series in Applied Mathematics, Society for Industrial and Applied Mathematics, 2014.
- [48] P.-G. MARTINSSON, *A direct solver for variable coefficient elliptic pdes discretized via a composite spectral collocation method*, Journal of Computational Physics, 242 (2013), pp. 460–479.
- [49] P. G. MARTINSSON AND V. ROKHLIN, *A fast direct solver for boundary integral equations in two dimensions*, Journal of Computational Physics, 205 (2005), pp. 1–23.
- [50] C. C. PAIGE AND M. A. SAUNDERS, *Lsqr: An algorithm for sparse linear equations and sparse least squares*, ACM Transactions on Mathematical Software (TOMS), 8 (1982), pp. 43–71.
- [51] M. J. POWELL, *A hybrid method for nonlinear equations*, Numerical methods for nonlinear algebraic equations, (1970), pp. 87–144.
- [52] ———, *A new algorithm for unconstrained optimization*, in Nonlinear programming, Elsevier, 1970, pp. 31–65.
- [53] V. ROKHLIN, *Solution of acoustic scattering problems by means of second kind integral equations*, Wave Motion, 5 (1983), pp. 257–272.
- [54] M. SINI, N. T. THANH, AND W. RUNDELL, *Inverse acoustic obstacle scattering using multi-frequency measurements*, Inverse Problems & Imaging, 6 (2012).

- [55] N. T. THANH, L. BEILINA, M. V. KLIBANOV, AND M. A. FIDDY, *Reconstruction of the refractive index from experimental backscattering data using a globally convergent inverse method*, SIAM Journal on Scientific Computing, 36 (2014), pp. B273–B293.
- [56] E. USTINOV, *Encyclopedia of Remote Sensing*, Springer New York, New York, NY, 2014, ch. Geophysical Retrieval, Inverse Problems in Remote Sensing, pp. 247–251.
- [57] J. XIA, S. CHANDRASEKARAN, M. GU, AND X. S. LI, *Fast algorithms for hierarchically semiseparable matrices*, Numerical Linear Algebra with Applications, 17 (2010), pp. 953–976.
- [58] L. ZEPEDA-NÚÑEZ AND H. ZHAO, *Fast alternating bidirectional preconditioner for the 2d high-frequency lippmann–schwinger equation*, SIAM Journal on Scientific Computing, 38 (2016), pp. B866–B888.